Dissolution-driven propulsion of floating solids

Martin Chaigne $^{\rm a,2}$, Michael Berhanu $^{\rm a,1,2}$, and Arshad Kudrolli $^{\rm b,1,2}$

^aMSC, Université Paris Cité, CNRS (UMR 7057), F-75013 Paris, France; ^bDepartment of Physics, Clark University, Worcester, Massachusetts 01610, USA

This manuscript was compiled on June 29, 2023

11

12

13

14

17

19

21

20

21

We show that unconstrained asymmetric dissolving solids floating in a fluid can move rectilinearly as a result of attached density currents which occur along their inclined surfaces. Solids in the form of boats composed of centimeter-scale sugar and salt slabs attached to a buoy are observed to move rapidly in water with speeds up to 5 mm/s determined by the inclination angle and orientation of the dissolving surfaces. While symmetric boats drift slowly, asymmetric boats are observed to accelerate rapidly along a line before reaching a terminal velocity when their drag matches the thrust generated by dissolution. By visualizing the flow around the body, we show that the boat velocity is always directed opposite to the horizontal component of the density current. We derive the thrust acting on the body from its measured kinematics, and show that the propulsion mechanism is consistent with the unbalanced momentum generated by the attached density current. We obtain an analytical formula for the body speed depending on geometry and material properties, and show that it captures the observed trends reasonably. Our analysis shows that the gravity current sets the scale of the body speed consistent with our observations, and we estimate that speeds can grow slowly as the cube-root of the length of the inclined dissolving surface. The dynamics of dissolving solids demonstrated here applies equally well to solids undergoing phase change, and may enhance the drift of melting icebergs, besides unraveling a primal strategy by which to achieve locomotion in active matter.

fluid-mechanics | self-propulsion | dissolution | natural convection | fluid-structure interaction

Self-propulsion by converting stored energy into mechanical motion is at the heart of active matter (1). The motion may occur through a chemical reaction enabling ciliary beating in micro-swimmers (2–4), or by generating ballistic motion at molecular scales by catalytic boosts of enzymes (5). At the granular scale, directed motion can be observed on vibrating substrates via spontaneous symmetry breaking (6) or more robustly with polar grains (7). Self-propulsion can also be created without mechanical action. For example, asymmetric particles which catalyze a chemical reaction in the fluid can break mechanical equilibrium (8). Chemical or temperature gradients can also induce variations of the surface tension on droplets generating propulsion due to the Marangoni effect (9–12), and Leidenfrost droplets can experience propulsion caused by interactions with the substrate (13–15).

Density currents resulting from spatial variations in fluid density constitute another possible mechanism for self-propulsion. This mechanism, which is not restricted to a free-surface as in the Marangoni effect and is not limited to microscopic scales, has received limited attention. Passive asymmetric solids floating in density stratified fluids have been reported to experience thrust leading them to move slowly with speeds of a few microns per second (16). Faster transport can occur if the body itself generates density variation in the surrounding fluid as demonstrated by Mercier, et al. (17) with a floating asymmetric solid with an embedded local heat source

that generates thermal convection. However, convective flow can also occur without an added heat-source through the progressive phase change of a solid immersed in a fluid. Gravity currents due to solute concentration gradients have been studied to understand shapes changes in dissolving solids (18–22), but whether these flows lead to self-propulsion of the solid itself was unprobed. While auto-rotation of floating ice disks caused by melting has been noted (23), net translation was not noted in these studies. More recently, dissolving colloidal particles driven by Brownian motion have been considered theoretically and predicted to undergo stochastic dynamics (24), but any effect of convective flow of the surrounding fluid as a result of the dissolution was not examined.

31

32

33

34

35

36

37

38

39

40

41

42

43

46

47

48

49

50

51

53

54

Here, we show that an unconstrained asymmetric dissolving solid can propel itself rectilinearly because of the thrust generated as a reaction to the unbalanced momentum of the solute-rich density current which develops along its inclined surfaces. While we focus here on the case of dissolution because it does not have the complexity associated with temperature gradients and phase change, the elucidated propulsion mechanism applies equally well to asymmetric bodies undergoing melting. We further discuss the implication for active transport of floating ice as a result of melting or freezing, relative to their advection due to wind and ocean currents (25–28).

1. Results

A. Design and observations. We construct dissolving bodies in the form of boats which float asymmetrically in water by attaching a solid $7.5 \times 4.0 \times 0.5 \, \mathrm{cm}^3$ rectangular candy slab to the bottom of a hollow plastic box which acts as a buoy. A

Significance Statement

Gravity driven turbulent flows are well known to occur because of solute concentration gradients, but the fact that an untethered dissolving body can translate robustly as a reaction to such flows has not been demonstrated. By constructing sugar and salt boats, we show that an inclined floating body can self-propel rapidly as it dissolves. The velocities achieved with such flows can be at least an order of magnitude faster compared with those with laminar flows, and thus our results broaden the conditions under which natural convection can give rise to translation motion of immersed bodies. This propulsion mechanism can apply equally to melting or freezing solids and represents an elemental mechanism by which matter can move actively.

M.C. and M.B. designed study, constructed apparatus, collected data, developed thrust model and analysis, and wrote paper. A.K. designed study, developed analysis, and wrote paper.

The authors declare no competing interest.

¹ M.B. (Author Two) and A.K. (Author Three) contributed equally to this work

²To whom correspondence should be addressed. E-mail: martin.chaigne@u-paris.fr michael.berhanu@u-paris.fr; akudrolli@clarku.edu

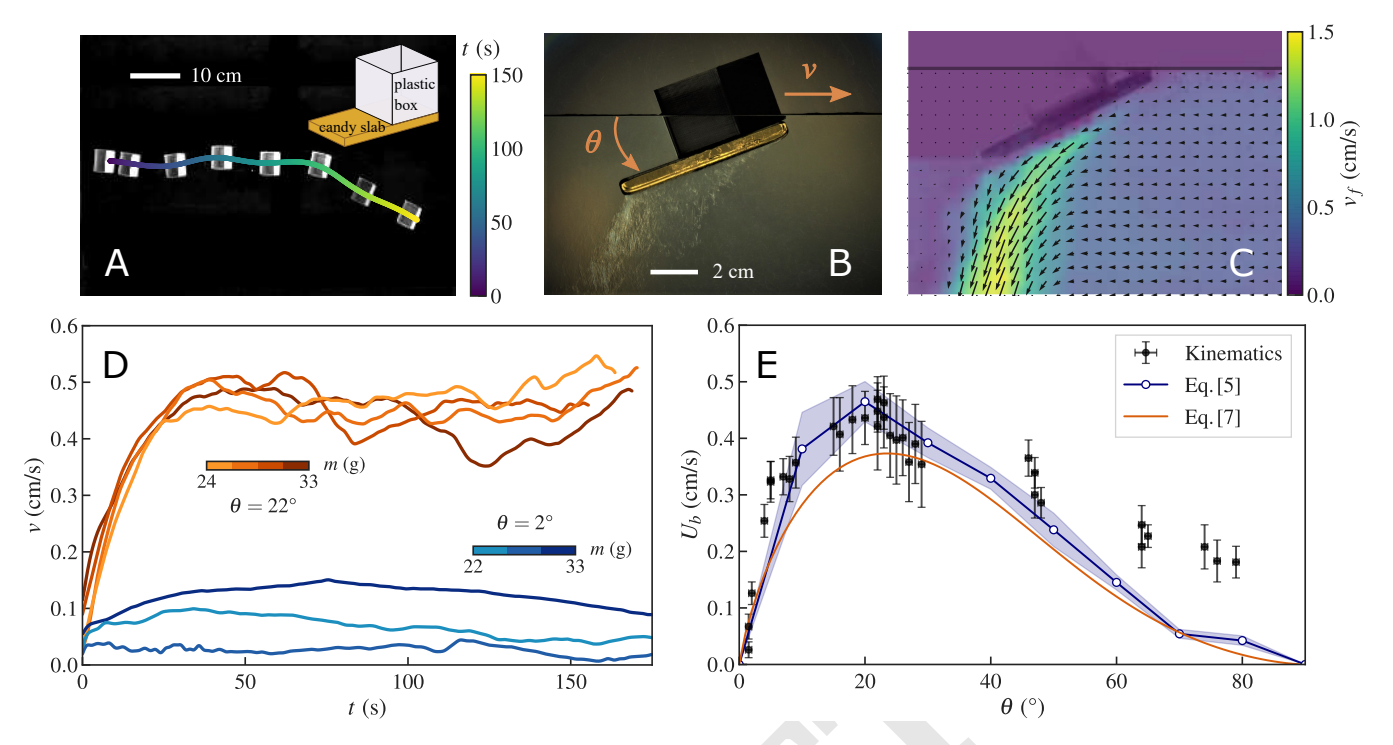


Fig. 1. Kinematics of the candy boats. A: Superimposed images at $20 \, \mathrm{s}$ time intervals show the motion of a candy boat in a large tank of water (top view). Inset: Schematic of a candy boat. B: An image of a candy boat moving in water obtained with shadowgraph technique (side view). Solute-rich plumes are visible descending below the dissolving boat. C: The fluid velocity v_f in the body frame of reference measured with PIV in the mid-vertical cross-section of the boat superimposed on an image of the system $(\theta = 26^{\circ} \pm 1^{\circ})$. The magnitude and direction of v_f averaged over 15 seconds are shown with arrows and color map. D: The evolution of boat velocity v corresponding to consecutive launches with two different boats: $\theta = 22^{\circ} \pm 1^{\circ}$ (orange lines) and $\theta = 2^{\circ} \pm 1^{\circ}$ (blue lines). The mass m decreases with each trial and is shown by color bar for each boat. E: The measured boat speed U_b (\bullet) varies significantly with θ , and is well described by estimates obtained by performing a momentum balance analysis (Eq. [5]) with measured flow fields in Section 2, and by the functional analysis which leads to Eq. [7] combined with Eq. [8] in Section 3. The blue shade corresponds to the estimated error in determining F_b^{MB} . Systematic deviations are observed at higher θ because only the contribution of the flow below the dissolving slab is considered for simplicity of analysis.

schematic of such a candy boat is shown in the Inset to Fig. 1A and further details on its fabrication process can be found in the Methods section. When the composite boat floats in water, the placement of the buoy relative to the center of the heavier candy slab determines the inclination angle θ of the dissolving surfaces as shown in Fig. 1B. In all, a set of 9 boats with mass m of approximately 33 g each were constructed with identical dissolving slabs and buoys to vary θ between 0° and 80°, and to study the effect of breaking fore-aft symmetry on their dynamics.

Figure 1A and SI Movie S1 show a time-sequence of a dissolving solid boat corresponding to $\theta=22^{\circ}$ moving in fresh water after it is released from rest in a large tank. We observe from the superimposed trajectory of the candy boat that it moves essentially rectilinearly while achieving speeds of order 5 mm/s. By contrast, we observe that the boat drifts slowly with speeds less than 0.7 mm/s if the plastic hull is placed centrally which results in $\theta\approx2^{\circ}$ (see SI Movie S2). Thus, symmetry breaking due to the inclination of the dissolving body is important to the observed rapid rectilinear motion.

We further visualize the solvent bath to examine the soluterich fluid which occurs around the dissolving body. The images shown in Fig. 1B and SI Movie S3 are taken with shadowgraph technique which magnifies refractive index variations caused by the solute concentration. Turbulent plumes are observed to emerge directed behind and below the dissolving surface as the boat moves forward, but the area near the air-water interface around the boat does not show any refraction due to

the presence of solute which may signal surface tension gradients. We further visualize the fluid motion with Particle Image Velocimetry (PIV) by adding fluorescent tracers as discussed in SI Section 1. PIV measurements. Fig. 1C shows the corresponding flow field v_f obtained with PIV in a vertical cross sectional plane. To our knowledge, the convection flow below a dissolving body has not been quantitatively characterized previously. The fluid can be observed to accelerate rapidly below the inclined dissolving surface before detaching and flowing downwards with the greatest velocities directed below and behind the dissolving surface. Because the solute-rich fluid descends rapidly to the bottom of the tank, the fluid near the surface remains solute-free, since the fluid is drawn in apparently faster than the time scale over which the solute can diffuse out around the dissolving solid. Thus, the boat is seen to move opposite to the direction of the density current which flows towards the back, while moving down due to the action of gravity.

By adding weights to the plastic box, we submerged the entire body to a depth of 4 cm, turning it into a submarine. To maintain a constant immersion depth, a stratified bath was prepared with a fresh water layer lying over a denser salt water layer (for more details see SI Section 2. Fully submerged body). We observe that the boat moves similarly as shown in SI Movie S4 with speeds up to 1 mm/s, roughly the same order of magnitude as when floating at the air-water interface. This observation further confirms that the propulsion mechanism at play is different from Marangoni flows which can propel

87

88

89

90

91

94

95

97

100

101

104

105

106

107

57

59

60

61

62

63

64

65

66

67

68

71

72

73

74

75

77

78

79

80

dissolving solids such as camphor boats due to surface tension gradients (29-31).

112

113

114

115

117

118

119

120

121

122

124

125

126

127

128

129

131

132

133

134

135

137

140

141

142

143

144

145

146

147

148

149

150

151

152

153

154

155 156

157

158

159

160

161

162

163

164

165

166

167

168

169

170

172

We also performed measurements with dissolving boats where the sucrose block was replaced with a salt (NaCl) block with dimensions $4.1\,\mathrm{cm}\times2.3\,\mathrm{cm}\times0.6\,\mathrm{cm}$ to test whether the propulsion can be observed with other dissolving materials. The same qualitative behavior is observed with $U_b\approx4.2\,\mathrm{mm/s}$ when $\theta=40^\circ$ (see SI Section 3. Effect of Dissolving Material). Unlike sugar-water solutions where viscosity can vary several orders of magnitude when the saturation limit is reached, the viscosity of saturated salt solution is only higher by a factor 2 compared with water (32). Thus, the large viscosity variations specific to sugar solutions do not play an appreciable role in the propulsion.

To further check the robustness of the propulsion mechanism, and its persistence in multi-body environments, we performed experiments with two candy boats with the same length $L=7.5\,\mathrm{cm}$, and $\theta=33^o\pm2^o$. As shown in SI Movie S5, when the boats are moving in a row in the same direction, the following boat catches up with the leading boat, and the boats self-assemble to move forward in tandem. While approaching from opposite directions, the boats come in contact, pair up, and then spin around each other as shown in SI Movie S6 and SI Movie S7, with speeds that depend on their relative contact position (see SI Section 4. Boat Pairs). Thus, we find that while capillary interactions, important over the scale of a centimeter or less (33, 34), cause these bodies floating at the surface to stay in contact, it is clear that such boats can move collectively and can show further rich phenomena.

B. Kinematics. Figure 1D shows the measured boat velocity vobtained from the displacement of its center of mass position over a time interval of $0.2 \, \mathrm{s}$ as a function of time t corresponding to $\theta = 22^{\circ}$. Four consecutive launches of the same boat are shown to illustrate the robust features of the kinematics. We observe that v increases smoothly before the turbulent nature of the plumes and rudderless nature of the boat causes its velocity to fluctuate somewhat randomly. The total mass of the boat is observed to decrease by approximately 10% over the course of the entire trial. Since θ depends on the relative mass and location of the buoy and the heavier dissolving block, it can evolve slowly over time in principle with dissolution. However, the measured θ was observed to be constant to within 1° in these examples, and no systematic variation from one launch to the next can be observed. We obtain the boat cruising speed $U_b \approx 4.5 \,\mathrm{mm/s}$ by averaging over the time after the boat stops accelerating forward (about $t = 40 \,\mathrm{s}$ here), and while it maintains a more or less constant speed. These observed speeds are faster by an order of magnitude compared with previous demonstrations of temperature-gradient driven convective transport in immersed bodies (17), and more than two orders of magnitude faster than diffusion-driven transport in stratified fluids (16).

We investigate U_b further as a function of the inclination of the dissolving surfaces using the nine different candy boats constructed with different buoy locations. Figure 1E shows the mean U_b and θ along with their standard deviations for a given trail. We observe that U_b increases rapidly reaching a peak at $\theta \approx 22^{\circ}$, before decreasing as θ increases toward 80°. The overall increase and then decrease of speed with θ is consistent with the rectangular geometry of a dissolving block which would be symmetric about the vertical axis, when $\theta = 0^{\circ}$ and

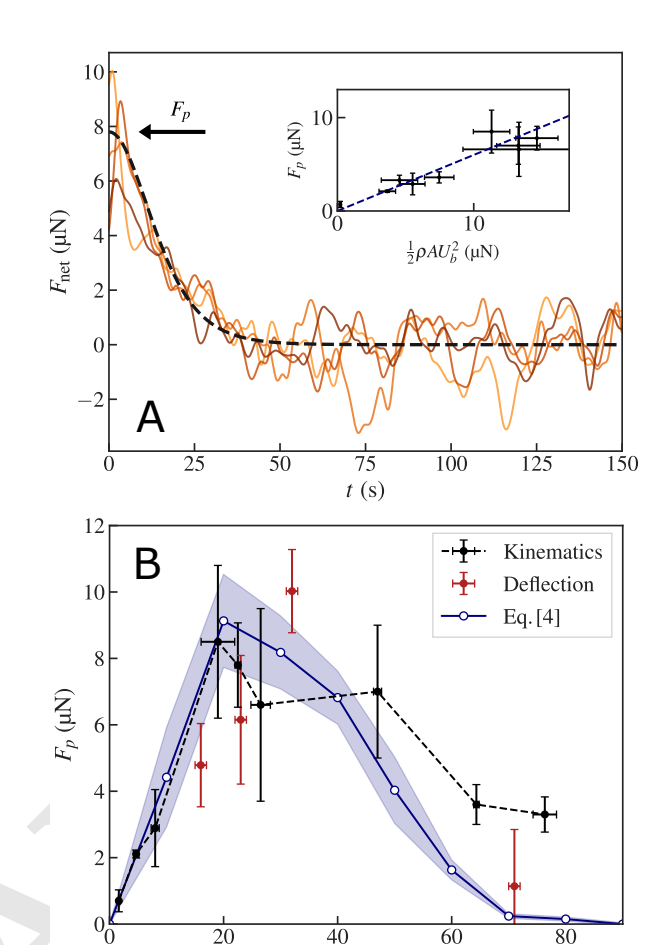


Fig. 2. Forces acting on a moving dissolving body. A: The net force $F_{\rm net}$ decays to zero as the drag increases with speed and balances the thrust F_p . The dashed line corresponds to Eq. [S2] assuming v^2 -drag (see SI text 4). Inset: F_p versus $F_d/C_d = \frac{1}{2} \rho L_A W U_b^2$. The data is described by a linear fit corresponding to quadratic-drag with $C_d = 0.6$. B: The thrust F_p obtained using kinematic measurements, deflection measurements, and calculated using the momentum balance condition given by Eq. [4], and its estimated error (blue shade).

 90° . Thus, the significant dependence of speed on θ highlights the importance of orientation of the dissolving surfaces on the propulsion of the dissolving bodies in our experiments.

173

174

175

177

178

179

180

181

182

183

184

185

186

187

188

189

190

C. Thrust and Drag. We examine the forces acting on the floating body as it dissolves, toward understanding its kinematics. Because the identification of distinct portions of the body over which the propulsive and the retarding forces apply is complex, we assume that the force exerted by the fluid on the boat is written as a constant term F_p , which we call "thrust", minus a term increasing with the velocity F_d , which we call "drag". Such a decomposition is widely used for example to model the kinematics of swimming bodies in the inertial regime (35–37), when the thrust and the drag result from a pressure field. The boat accelerates due to these unbalanced forces acting on it toward the bow along its symmetry axis. Neglecting the change in mass of the body, the net force $F_{\text{net}} = F_p - F_d$ is proportional to the acceleration of the body according to: $F_{\rm net} = m \, dv/dt$, where we ignore the added mass effect which may arise because moving a body requires displacing the fluid in which it is immersed (38–40). We plot $F_{\text{net}} = m \, dv/dt$ as

Dissolving Surface	Speed U_b (mm/s)	Area (cm ²)	h (mm/s)
Bottom and Top	3.3 ± 0.2	48	-
Bottom	2.6 ± 0.2	30	2.41×10^{-3}
Тор	0.5 ± 0.2	18	0.87×10^{-3}

Table 1. Measured mean speed U_b and its standard deviation corresponding to the exposed dissolving surfaces of the dissolving slab ($\theta=45^{\rm o}$). The difference in surface area and dissolution rate can account for the relative contribution of the bottom and top surfaces on U_b .

a function of time in Fig. 2A, and observe that it is highest close to $t=0\,\mathrm{s}$, when $v\approx0\,\mathrm{mm/s}$. F_{net} then decreases rapidly toward zero as drag increases and balances the thrust. When $v\to0$, we have $F_d\to0$ and $F_{\mathrm{net}}\to F_p$. We plot F_p as a function of θ in Fig. 2B, and observe that it increases and decreases with θ following the trends in U_b with θ . We performed further complementary measurements of F_p by obstructing the boat's forward motion using a long thin rod and measuring its deflection (see Fig. 2B). The measured thrusts using the two methods are in overall agreement, confirming that the added mass effect can be neglected at least at low to moderate θ .

If the thrust does not change with v, we have $F_d = F_p$ when the boat moves with speed U_b . The drag can be written in general as $F_d = \frac{1}{2}C_d\rho_f A U_b^2$, where $\rho_f = 997 \,\mathrm{g} \,\mathrm{L}^{-1}$ is the density of water, A is the projected area along the direction of the boat's velocity, and C_d is the drag coefficient. We have A = $L_A W$, where W is the width and L_A is the projected length measured for each boat from a side view image corresponding to the projected length of its immersed part on the vertical axis (see SI Section 5. Projected Boat Length). The Reynolds Number over the scale of the boat can be estimated as Re = $U_b L/\nu \approx 340$, since L = 7.5 cm, $U_b \approx 4.5$ mm/s and $\nu =$ 1.00×10^{-6} m² s⁻¹, the kinematic viscosity of water at 20°C. Since $Re \gg 1$, the drag can be expected to scale quadratically with speed. We plot F_p versus $F_d/C_d = \frac{1}{2}\rho L_A W U_b^2$ in the inset of Fig. 2A, where each point represents averaged values over trials of the same boat. The data is observed to be well described by a linear fit, with a slope corresponding to $C_d = 0.6$, which is reasonable considering C_d for a nonstreamlined body (38).

We calculate an analytical expression for $F_{\rm net}$ over time assuming thrust F_p independent of v, and $F_d = \frac{1}{2}C_d\rho Av^2$ in SI Section 6. Net Force Evolution. Plotting $F_{\rm net}$ using the measured ratio $C_d = 0.6$ in Fig. 2A (dotted line), we find good agreement with the time scales over which the boat accelerates. This agreement validates our assumption that the thrust generated by the dissolution is essentially independent of the speed of the boat, and depends only on the angle of inclination of the dissolving surface. Even though it is not obvious in general, the agreement also confirms a posteriori the decomposition of forces into thrust and drag on the same surface. Thus, we find that a dissolving body released from rest accelerates and reaches a cruising velocity as its drag increases and matches the thrust corresponding to its geometry.

D. Effect of dissolving surface orientation. We gauge the relative effect of the upward and downward facing surfaces of the dissolving slab on the propulsion speed by adding a thin plastic wing to the side of the plastic box such that the dissolving slab is covered from above or below. The measured speeds are given in Table 1 corresponding to $\theta = 45^{\circ}$. While

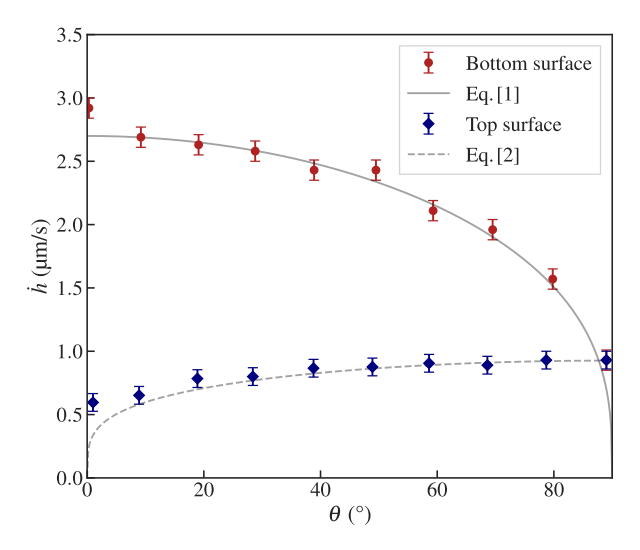


Fig. 3. The measured recession rate \dot{h} along the top and bottom surface of the dissolving block as a function of its inclination angle θ . Grey lines: Calculated recession rates at the bottom surface (Eq. [1], solid line), where a density inversion instability leads to faster \dot{h} , with $Ra_c=1101$ and $\nu_i=2.5\times 10^{-4}\,\mathrm{m^2\,s^{-1}}$, and at the top surface (Eq. [2], dashed line) with fitting parameter $B=1.15\times 10^{-4}\,\mathrm{cm^{5/4}\,s^{-1}}$ (42). Greater boat speeds are observed when the bottom surface dissolves compared to top surface at the same inclination angle.

the greatest speed is achieved when both the top and bottom surfaces of the slab are allowed to dissolve, U_b is about 5 times greater when the bottom surface is exposed compared to the top surface. The presence of the buoy screens part of the slab resulting in the area of the bottom surface being nearly 2 times larger than the top surface. Thus, while part of the greater contribution of the bottom surface is due to its larger surface area, bottom facing surfaces dissolve faster than top facing surfaces (41).

To ascertain the effect of inclination on the dissolution of the body and its effect on U_b , we measure the location and evolution of the dissolving surface at various θ . Figure 3 shows the recession rate \dot{h} of the dissolving surface as a function of its orientation. Because of the solutal Rayleigh-Bénard instability, \dot{h} is greatest when $\theta=0^{\circ}$, but decreases as θ increases when the dissolving surface faces down.

The recession rate \dot{h} can be calculated based on material properties and the inclination of the dissolving surface. In the presence of solutal convection (41), $\dot{h} = \frac{D \, \rho_{sat} \, c_{sat}}{\rho_s \, \delta_c \, (\rho_{sat} - c_{sat})}$, where ρ_s is the density of the dissolving solid, ρ_{sat} is the saturation density of the solute, c_{sat} is the saturation concentration, D is the diffusion coefficient, and δ_c is the concentrated solute boundary layer thickness (see SI Section 7. Surface Recession Rates). When the surface is oriented downward, the boundary layer is subject to a Rayleigh-Bénard instability. In the quasistationary regime, δ_c is set by the critical Rayleigh number $Ra_c \, (18-20)$. The effect of the inclination can be taken into account by considering the projection of the gravity perpendicular that the country $\delta_c \, (18-20)$ are $\delta_c \, (18-20)$.

ular to this layer (21). Then,
$$\delta_c = \left(\frac{Ra_c \nu_i \rho_f D}{g\cos\theta \left(\rho_{sat} - \rho_f\right)}\right)^{1/3}$$
, where Ra_c can be approximated as 1101 in case of a Rayleigh-Bénard instability in a layer with mixed slip and non-slip boundary conditions (43), ρ_f is the density of the far field liquid and ν_i is the average viscosity of the boundary layer.

Thus, the recession rate at the bottom surface is:

277

280

281

282

283

287

288

289

290

292

293

294

295

296

297

298

299

300

301

302

303

304

305

306

307

308

309

310

311

312

316

317

318

319

320

323

324

325

$$\dot{h}_b = \frac{\rho_{sat} c_{sat} D^{2/3}}{\rho_s (\rho_{sat} - c_{sat})} \left(\frac{g \cos \theta (\rho_{sat} - \rho_f)}{Ra_c \nu_i \rho_f} \right)^{1/3}.$$
[1]

We evaluate \dot{h}_b using the parameters corresponding to sucrose dissolving in fresh water, where $\rho_s = 1430\,\mathrm{g\,L^{-1}}$, $\rho_f = 997\,\mathrm{g\,L^{-1}}$, $\rho_{sat} = 1300\,\mathrm{g\,L^{-1}}$, $c_{sat} = 940\,\mathrm{g\,L^{-1}}$, $D = 4.3 \times 10^{-10}\,\mathrm{m^2\,s^{-1}}$, and $\nu_i = 2.5 \times 10^{-4}\,\mathrm{m^2\,s^{-1}}$ by interpolating between the saturation concentration $\nu_s = 7.7 \times 10^{-4}\,\mathrm{m^2\,s^{-1}}$ and the fresh water $\nu = 1.0 \times 10^{-6}\,\mathrm{m^2\,s^{-1}}$ (19, 41). A comparison is plotted in Fig. 3, and good agreement is observed.

At the top surface of the slab, the convection is gravitationally stable, and one can obtain (see SI Section 7. Surface Recession Rates) an expression for dissolution rate averaged over the length of the dissolving surface as:

$$\dot{h}_t = \frac{4B\sin\theta^{1/4}}{3L^{1/4}},\tag{2}$$

where B is a material dependent fitting parameter. This expression is also plotted in Fig. 3, and observed to describe the data reasonably, except near $\theta = 0^{\circ}$, because the expression is valid only for sufficiently inclined surfaces that give rise to a slope-driven buoyancy flow (42).

Thus, the body dissolving asymmetrically with θ with density inversion instability leads to faster dissolution at the bottom surface, which in turn leads to faster U_b . At $\theta = 45^{\circ}$, \dot{h} is approximately 2.5 times higher at the bottom surface compared to the top surface. This factor along with the difference in surface area partly explains the nearly 5 times higher speeds recorded when the bottom versus top surfaces alone are allowed to dissolve as noted in Table 1.

2. Propulsion mechanism

To explain the motion of the dissolving body, we hypothesize that the solute rich density current creates a pressure difference fore and aft of the immersed body giving rise to the thrust needed to accelerate the body from rest (the direct thrust due to the dissolution of mass at a rate given by h can be calculated to be negligible as shown in SI Section 8. Estimate of thrust due to direct solute dissolution). When the dissolving surface is located above the solvent, the solute-rich fluid layer is susceptible to a solutal density inversion instability (41). As seen in the shadowgraph image Fig. 1B, the dense fluid does not sink strictly vertically. The gravity-driven current acquires a horizontal component due to a suction effect. Low pressure is created at the bottom face of the slab due to the sinking plumes which causes the boundary layer to remain attached to the surface, while gravity causes it to flow downwards. Thus, the flow must have a horizontal component, directed backwards relative to the boat. The forward motion of the boat can then be seen in two ways, which are ultimately equivalent, in terms of force or in terms of momentum: either as the result of the net flow directed backwards, or as the result of the low pressure region located along the candy slab which induces a net horizontal force. While buoyancy rapidly ensures vertical balance, the solid is pulled horizontally by the low-pressure region in the direction opposite to the horizontal component of the sinking fluid, providing the propulsion mechanism. If the dissolving surface is located below the solvent, the solute-rich fluid follows the inclined surface in a barely visible thin layer due to unbalanced gravitational force when $\theta > 0$, and is ejected off to the sides as it falls over the inclined dissolving slab. Such a flow would give rise to reaction forces which would further contribute to the propulsion of the boat. Since the downward facing surface dissolves faster and makes a dominant contribution to the observed speed as discussed in Section 1D, we only focus on the region below the dissolving slab to develop a simplified quantitative understanding of the thrust which accelerates the boat.

331

332

333

334

335

337

338

339

340

341

342

343

344

346

347

348

349

350

351

352

353

355

356

357

358

359

360

364

365

366

367

368

369

371

372

373

374

375

376

379

380

381

382

383

384

385

A direct evaluation of the pressure field on the solid wall is difficult because of the intermittent nature of the plumes and the complex flow geometry. Therefore, we employ an approach using momentum balance to calculate the thrust from the measured mean velocity field near the dissolving solid. When the boat moves with constant velocity it is not possible to evaluate thrust using the flow field because the thrust equals drag in that limit. However, the thrust can be evaluated from the flow field around a stationary boat, since the thrust remains independent of speed according to Fig. 2A. Therefore, we perform a series of measurements of the flow field below an identical dissolving slab held at rest with various θ .

Fig. 4A-C shows examples of observed flow fields at low, intermediate, and high inclination angles, respectively, obtained with PIV. We observe that the overall flow is more or less downward along gravity at small θ , but becomes increasingly attached to the dissolving surface with increasing θ . The asymmetry of the slab thus leads the flow to acquire a strong lateral component: this, in addition to being an interesting discovery in itself, is crucial for propulsion. The main features of the solute-rich fluid flow are schematically represented in Fig. 4D, where a steady flow with velocity v_p is directed along the dissolving surface. We denote δ_v the thickness over which the flow velocity decreases to half its value. We estimate v_p from the measurements through the horizontal surface below the dissolving body bounded by the x_1 and x_2 planes, and plot it in Fig. 4E as a function of θ . We observe that v_p increases rapidly as the inclination of the dissolving slab is increased from $\theta = 0^{\circ}$, and reaches a peak over a similar range as U_b , before decreasing as the dissolving surface becomes vertical. Further, we plot the projection δ_x of the rapidly flowing layer δ_v on the axis between x_1 and x_2 scaled by L in Fig. 4F. δ_x decreases monotonically with θ , and is well described by the empirical form:

$$\frac{\delta_x}{L} = \frac{1}{2}\cos^2\theta. \tag{3}$$

It can be noted that $\delta_x = L/2$ when $\theta = 0^{\circ}$, meaning that the width of the rapid current below a horizontal slab is only half that of the slab. Then, δ_x/L decreases when θ increases since the flow becomes increasingly narrow and attached to the slab.

Hence, we consider the prismatic volume V, below the inclined dissolving surface, as illustrated in Fig. 4D, bounded by the dissolving surface, the horizontal plane $z=z_1$, and the vertical planes $x=x_2$, $y=y_1$ and $y=y_2$ with $y_{1,2}=\pm W/2$. Assuming the fluid to be inviscid and incompressible, we obtain the horizontal component of the thrust acting on the dissolving surface considering momentum balance (38) along

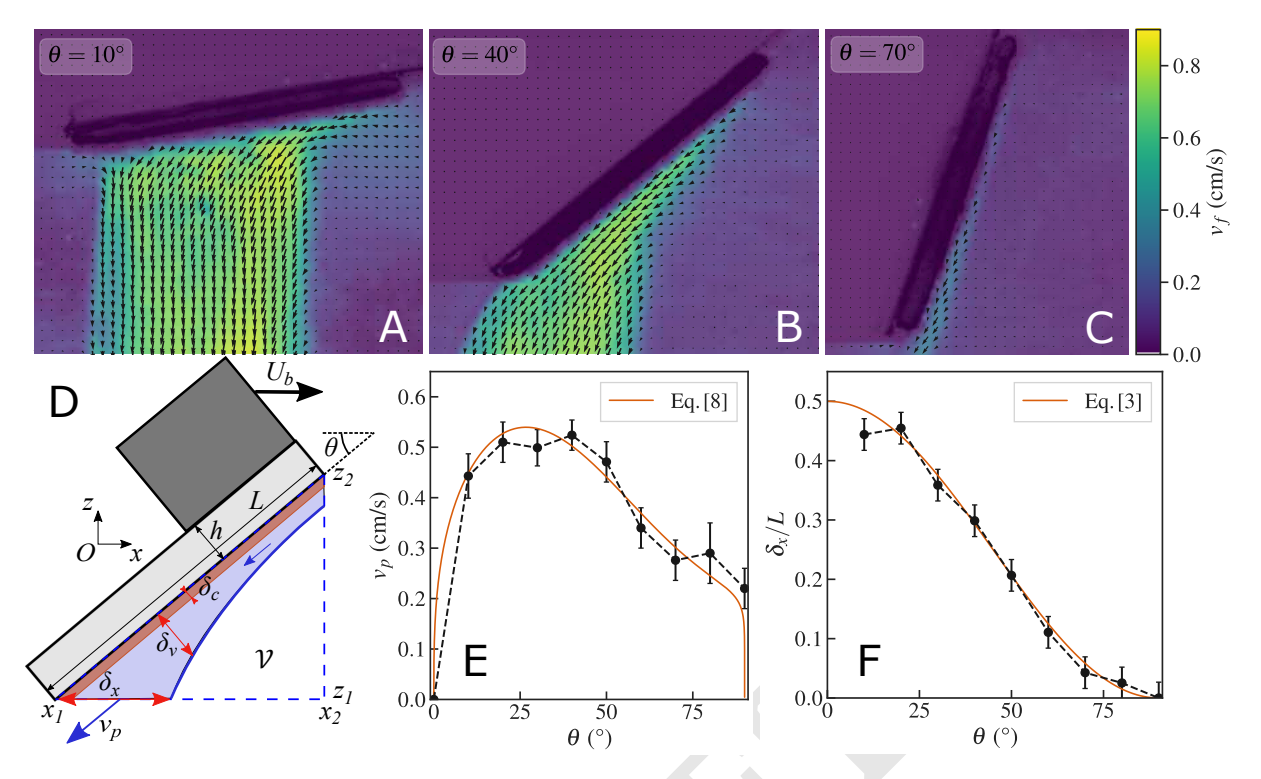


Fig. 4. Buoyancy driven flow characterization. A-C: Velocity field under the static candy plate at three different inclinations. D: A schematic of the main features of the flow in the vertical plane important to determining the thrust on the bottom surface of the dissolving slab. A prismatic volume $\mathcal V$, denoted by the blue dashed lines with lateral width W, below the dissolving surface is used in analyzing the momentum balance. The flow leaving $\mathcal V$ through the bottom side is mostly confined over a length δ_x and has a magnitude v_p . The rapid flow is confined over a distance δ_v perpendicular to the dissolving surface, and δ_c is the thin nearly saturated solute boundary layer. E: Plot of v_p , corresponding to the maximal value of the parallel component of the fluid velocity at $z=z_1$ between x_1 and x_2 , as a function of θ . Solid orange line corresponds to a theoretical estimation according to Eq. [8], with a dimensionless prefactor of order one depending on the angle chosen to fit the data (see SI Section 11. Inverse Friction coefficient and Fig. S9). F: The effective width of the rapid flow δ_x/L versus θ . Solid orange line corresponds to empirical formula given by Eq. [3].

the horizontal x-axis as

$$\begin{split} F_p^{MB} &= -\int_{y_1}^{y_2} \int_{z_1}^{z_2} \rho \, v_x^2 \, \mathrm{d}y \, \mathrm{d}z \,|_{x=x_2} \\ &+ \int_{z_1}^{z_2} \int_{x_1}^{x_2} \rho \, v_y \, v_x \, \mathrm{d}x \, \mathrm{d}z \,|_{y=y_1} \\ &- \int_{z_1}^{z_2} \int_{x_1}^{x_2} \rho \, v_y \, v_x \, \mathrm{d}x \, \mathrm{d}z \,|_{y=y_2} \\ &+ \int_{y_1}^{y_2} \int_{x_1}^{x_2} \rho \, v_z \, v_x \, \mathrm{d}y \, \mathrm{d}x \,|_{z=z_1} \,, \end{split} \tag{4}$$

where ρ is the fluid density, v_x , v_y , and v_z are the respective velocity components along the x, y and z axes as defined in Fig. 4D. The terms on the right hand side correspond to the fluid entering \mathcal{V} through vertical plane $x=x_2$, bounding vertical planes $y=\pm W/2$, and leaving through the bottom horizontal plane $z=z_1$. Because the mass of dissolved solute is negligible compared to the mass of the fluid, we evaluate each term separately assuming that ρ is given by the density of fresh water ρ_f in \mathcal{V} (see SI Section 9. Estimate of thrust from momentum balance). We find that the term corresponding to bottom plane dominates over the entire range of θ (see SI Section 10. Relative thrust contributions and Fig. S8). Thus, F_p is positive, in agreement with the direction of the acceleration when the body is released.

We compare the calculated magnitude of F_p^{MB} using Eq. [4] with data as a function of θ in Fig. 2B, and we find that it is overall in agreement with the thrust obtained from both the kinematic as well as the deflection measurements. Thus, we conclude that momentum balance gives a reasonable description of the observed thrust needed to accelerate the body

from rest as seen in our experiments. While F_p^{MB} underestimates observed F_p obtained from the kinematics, this is to be expected since we neglect the contribution of the top surface to propulsion, which becomes relatively more important as θ increases.

We can further compare the predicted speeds according to momentum balance to those measured in the experiments using the fact that we have $F_p = F_d$, and $F_d = \frac{1}{2} C_d \rho_f A U_b^2$, when the boat moves with constant velocity. Then,

$$U_b^{MB} = \sqrt{\frac{2F_p^{MB}}{C_d \, \rho_f \, A}} \,.$$
 [5] 422

Figure 1E shows U_b^{MB} (blue line) compared with measured U_b corresponding to each trial with the 9 different boats. Good agreement is observed with U_b , except for $\theta > 60^\circ$, where contribution of the attached convection flow on the top of the dissolving slab may become significant. Thus, we find that the mechanism of propulsion based on the pressure variation produced by the attached sinking density current can capture the overall order of magnitude of the thrust acting on the dissolving body, and the speeds attained as a function of the inclination angle.

3. Functional analysis of boat speed

In order to understand the physical and geometrical parameters setting the boat velocity U_b beyond the propulsion mechanism, we further simplify the flow modeling. We only consider

the term corresponding to the flow through the bottom surface $z=z_1$ in Eq. [4], since it makes the dominant contribution to determine F_p (see SI Fig. S8). Further, measurements taken in the y-z plane (see SI Section 1. PIV measurements) show that the descending density flow is mainly confined to the central half-width of the dissolving surface. The flow out of z_1 is thus mostly confined over a region with length scale δ_x and width W/2, with an approximate flow velocity $v_x=v_p\cos\theta$ and $v_z=v_p\sin\theta$, and we have

$$F_p^{MB} \approx \rho_f \frac{W}{2} \, \delta_x \, v_p^2 \, \sin \theta \, \cos \theta \,.$$
 [6]

Then, using Eq. [5] and $A = L_A W$ (see section 1.C), we have

$$U_b^{th} = \sqrt{\frac{\sin 2\theta \, \delta_x}{2 \, C_d \, L_A}} \, v_p \,. \tag{7}$$

Thus, we observe the body speed is set by v_p besides other geometric factors related to the size and asymmetry of the floating body. Using Eq. [3] to express δ_x and Eq. [S1] to capture the measured dependency of the projected length L_A (see SI Section 5. Projected Boat Length), we find $\sin 2\theta \, \delta_x/L_A$ has a maximum at $\theta \approx 21^\circ$, which equals 0.58. Thus, we then find U_b^{th} is of similar order of magnitude as v_p at $\theta \approx 20^\circ$ from Eq. [7] since $C_d \approx 0.6$. This analysis which shows that the boat speed is of similar order of magnitude as the density current speed is consistent with our observations in Fig. 1E and Fig. 4E at intermediate θ .

We can estimate v_p itself by balancing the pressure difference which gives rise to the rapid flow below the dissolving slab, starting from (x_2,z_2) and ending at (x_1,z_1) , due to the non-buoyant weight of the solute-rich fluid with the drag as a result of inertial friction exerted by the quiescent fluid below and the dissolving surface above. Assuming that the shear occurs over length scale δ_v , we have $\Delta\rho\,g\,L\,\sin\theta=f_D\,\rho_f\,\frac{L}{\delta_v}\,v_p^2$, where $\Delta\rho$ is the increase in density due to the dissolved solute, and f_D is a dimensionless friction factor (38, 44). Using mass conservation of the solute, we have $\Delta\rho=\frac{\rho_s\,\dot{h}\,L}{\delta_v\,v_p}$, where ρ_s is the density of the dissolving solid, and \dot{h} is the recession rate of the dissolving surface given by Eq. [1]. Thus,

$$v_p = \mu_p \left(\frac{\rho_s g L \sin \theta \dot{h}}{\rho_f} \right)^{1/3},$$
 [8]

where $\mu_p=1/f_D^{1/3}$. Plugging in the values corresponding to where the maximum speed is observed $(\theta=22^\circ)$ in $v_p^o=\left(\frac{\rho_s\,g\,L\,\sin\theta\,\dot{h}}{\rho f}\right)^{1/3}$, we find that it is $10.1\,\mathrm{mm/s}$, comparable in magnitude to the measured $v_p=5.1\,\mathrm{mm/s}$. Thus, μ_p is a parameter which is of order 1. Because the geometry of the flow evolves with θ , μ_p is not constant. Thus, we plot the ratio v_p/v_p^o in Fig. S9, and find its dependence on θ . We plot Eq. [8] with the empirical value of μ_p as a function of θ in Fig. 4E. Hence we can estimate the value of U_b^{th} using Eq. [8], and the empirical forms for δ_x/L and L_A as a function of θ . We plot U_b^{th} versus θ in Fig. 1E (orange line), and observe that the estimated values follow the same trends as the data especially over low and intermediate inclination angles. U_b^{th} can be observed to be systematically increasingly lower with increasing θ . This trend is consistent with the expectation that

the flow near the top surface becomes increasingly important as θ increases toward 90°, although other assumptions in our model may contribute to these systematic deviations as well.

To test the robustness of the measurements and derived dependence further, we built additional boats with L between 7.5 cm and 2.6 cm. The data corresponding to each measured trail with the candy boats with various L is plotted in Fig. 5A versus the measured θ . Comparing U_b at similar θ , we note that speeds are lower for smaller L. To understand if this is consistent with our analysis, we combine Eq. [3], Eq. [7], Eq. [8], and the general expression of the erosion rate to obtain the following scaling after neglecting θ -dependence,

$$U_b^{th} \approx (D g)^{1/3} \left(\frac{c_{sat} \, \rho_{sat}}{\rho_f \left(\rho_{sat} - c_{sat} \right)} \right)^{1/3} \delta_c^{-1/3} L_A^{-1/2} L^{5/6}.$$
 [9] 487

The first term constitutes the intrinsic velocity scale of the system, and interestingly gives the right order of magnitude for the boat speed, i.e. $(D\,g)^{1/3}$ is of the order of 1.6 mm/s for sugar in water, and 2.5 mm/s for salt. Then, we can expect the explicit length dependence to scale as $L^{5/6}L_A^{-1/2}$, which reduces to $L^{1/3}$ when $L_A\approx L$ (see SI Section 12. Calculation of Boat Speed). Accordingly, we plot $U_bL^{-5/6}L_A^{1/2}$ versus θ in Fig. 5B, and find that the data collapse onto a common curve, showing that the length dependence is captured by our analysis. Here again, as in Fig. 1E, we observe that the theoretical curve given by Eq. [7] is systematically lower compared to the data by about 10% for $\theta < 45^{\circ}$, but the deviations become larger for higher inclinations with increasing $\theta > 45^{\circ}$ because only the contribution of the flow below the dissolving slab is considered in the model, and the contribution of the top surface increases.

In order to compare the measured and calculated speeds explicitly in the case of the various candy boats, but also the salt boat, we plot U_b versus U_b^{th} in Fig. 5C after substituting in Eq. [8] with the relevant physical, chemical and geometrical parameters. Except for the points corresponding to higher θ which lead to substantially lower U_b^{th} , we find that the data collapse close to the unit slope line. Thus, our model of the propulsion mechanism based on pressure difference caused by the rapidly descending density flow is consistent with our observations considering the approximations used to develop the analysis.

4. Discussions

In summary, we have demonstrated that an asymmetrically dissolving body can move rectilinearly with significant speeds while floating in a fluid. Robust directed motion is observed opposite to the principle direction in which boundary layer density currents are set up. We show that propulsion arises because of the differences in pressure fore and aft of the body due to the dense sinking current. The resulting horizontal unbalanced thrust accelerates the body till a constant velocity is reached when the thrust matches the body drag. The observed speed increases initially with inclination angle of the body, which leads to robust generation of gravity current due to break symmetry. The speed then decreases as the horizontal projection of the gravity current decreases with increasing angle leading to an optimal angle when the fastest speeds are observed. This observation of an efficient directed translation motion is in fact not obvious considering the relatively small mass loss rate and the intermittence of the flow. We also note

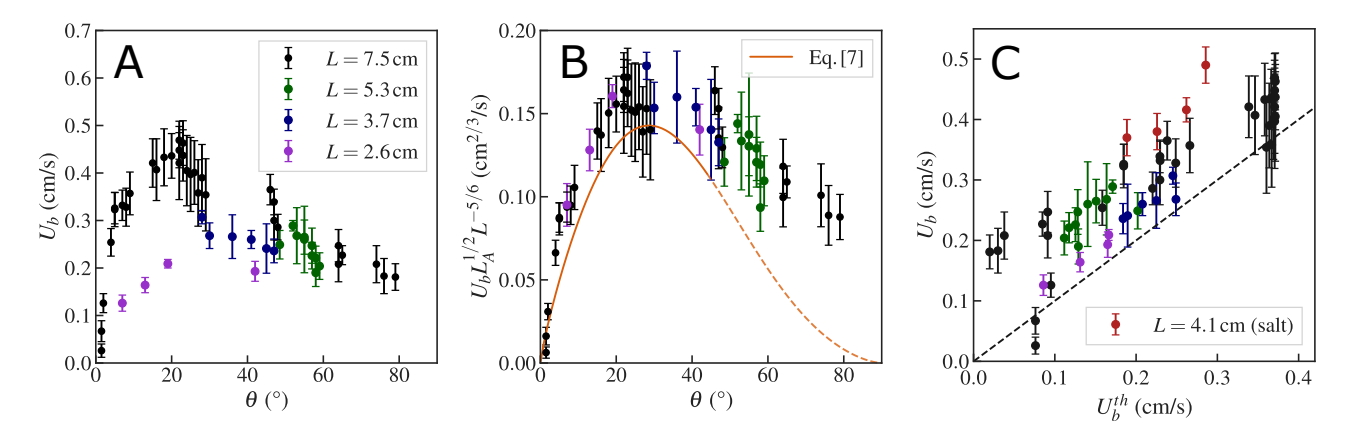


Fig. 5. Boat velocity for various sizes and comparison with model. A. Measured U_b corresponding to candy boats with various sizes as a function of θ . B. The data from the various boats collapse after scaling with L and L_A according implied scaling. Eq. [7] (solid orange line) matches the data at a 10% level for $\theta < 45^{\circ}$, but underestimate for higher θ (dashed orange line) because contributions of flows above the dissolving slab are not taken into account. C. Comparison of measured U_b and U_b^{th} (Eq. 7) corresponding to various candy and salt boats of various sizes. The trends are in overall agreement, with measured values being systematically higher compared to calculated values which only consider the contributions of flow below the boat in calculating the thrust.

that until this study, the convection flows generated by dissolution have not been quantitatively characterized and especially the presence of a horizontal net flow in the asymmetrical case has not been pointed out.

Even though the boundary layer is unstable and the density current is turbulent in our dissolution driven system, the underlying propulsion mechanism at work is similar to that observed in inhomogenously heated bodies that undergo translational motion due to stable laminar buoyancy currents (17). Thus, the propulsion mechanism is observed across different systems and can be applied to far stronger density currents which result in significantly faster rectilinear speeds. In particular, we find an order of magnitude higher speeds while considering similar centimeter-scale floating bodies, with even greater speeds estimated with increasing size. Considering observations with boat pairs, one can anticipate that capillary and hydrodynamic interactions can lead to collective phenomena such as self-assembly and swarming in dissolving boat clusters.

Because shape evolution due to melting and dissolution can be similar in solids (45,46), it is reasonable to consider whether discernible rectilinear transport can occur during melting or freezing of floating ice blocks due to temperature or salinity gradients (47,48). It has been shown that the melting of ice shelves generates upward buoyancy driving sub-glacial plumes before they break into icebergs (49). Similar plumes also occur at the immersed edges of icebergs. Recent models (50) estimate the plume thickness and their velocity to be about $10\,\mathrm{m}$ and $0.6\,\mathrm{m/s}$, respectively, for an iceberg of submerged height and width of $200\,\mathrm{m}$, under typical conditions observed in the polar regions of the Earth. Similar order of magnitudes are also obtained for plumes under ice shelves with a typical melting rate of $50\,\mathrm{m}$ per year (49).

While icebergs come in wide range of sizes, their shapes below the waterline are not known in much detail (51, 52). Except for tabular icebergs, the emerged part itself is rarely symmetric due to processes which lead to their formation and deterioration (53). Recent experimental works on the melting of vertical ice columns (54) have shown that vertical walls become inclined or scalloped in relation to buoyancy-driven flows with a slope sign depending on the water bath temper-

ature. Further, we have shown that even modest inclination leads to symmetry breaking of the boundary layer flow and directed motion. Therefore, using the corresponding values in the case of ice in place of v_p and $\delta_x \sin \theta$ in Eq. [6], we find $F_p \approx 7.0 \times 10^3 \,\mathrm{N}$. By comparison, a wind of moderate speed $U_W \sim 5$ m/s exerts on an exposed surface of area $S_a = 10 \times 200$ ${\rm m}^2$, a force $F_W \approx \rho_{air} S_a U_W^2 \approx 5 \times 10^4 {\rm N}$. This would imply a corresponding additional iceberg drift speed of approximately 2 cm/s. Thus a typical 200 m sized iceberg would move over its body length within about 3 hours. Such an appreciable effect should be measurable in the field by placing a couple of Global Positioning System (GPS) devices to track the location and rotation rate of a set of icebergs, while measuring the local wind and marine currents. The subsurface iceberg shape can be obtained with Ground-Penetrating Radar (GPR) (55), or with sonar placed on autonomous submarines (56). Then, by subtracting off the contributions of wind, currents, waves, and Coriolis force (25, 26, 57, 58), it may be possible to ascertain the importance of gravity-current driven propulsion by correlating them to rapidly melting icebergs with a statistically significant number of measurements. This would establish that contribution of ice melting on its drift may be not negligible, for a typical asymmetrical iceberg with inclined immersed walls. Thus, while wind and currents can lead to significant transport of sea ice and icebergs, density currents due to salinity gradients generated by iceberg melting, may in principle contribute to their transport as well.

Methods 6

A. Boat Construction. The boats are assembled by attaching a dissolving slab (dimensions $75\,\mathrm{mm}\times40\,\mathrm{mm}\times5\,\mathrm{mm}$, mass $\approx25\,\mathrm{g}$) to a hollow plastic box (dimensions $30\,\mathrm{mm}\times40\,\mathrm{mm}\times35\,\mathrm{mm}$ with $1.5\,\mathrm{mm}$ thick walls, mass $10\,\mathrm{g}$) with a thin layer of silicone sealant. Candy slabs are prepared following protocols used in previous studies (22, 41) to cast an inexpensive, homogeneous, reproducible and fast dissolving material with a prescribed shape. Rectangular shaped slabs are prepared by blending granulated sugar, light corn syrup and water starting with a 8:3:2 volume ratio. The mixture is then heated up to $150^{\circ}\mathrm{C}$ and poured into silicone molds with rectangular cross

sections, which after cooling result in solid slabs with requisite 612 dimensions. The plastic box is 3D-printed with PolyEthylene 613 Terephthalate (PET) filament with a Prusa 3D MK3S printer. 614 Additional experiments are performed with smaller slabs with 615 dimensions $53 \,\mathrm{mm} \times 27 \,\mathrm{mm} \times 5 \,\mathrm{mm}$, $37 \,\mathrm{mm} \times 20 \,\mathrm{mm} \times 5 \,\mathrm{mm}$ and $26 \,\mathrm{mm} \times 14 \,\mathrm{mm} \times 5 \,\mathrm{mm}$. The salt (NaCl) slab with dimensions $41 \times 23 \times 6$ mm is an optical rectangle window for 618 Infrared Spectroscopy obtained from Alfa Aesar. 619

B. Experimental Protocols. Experiments to measure speeds are performed in a rectangular $75 \times 45 \,\mathrm{cm}$ tank filled with distilled water to a depth of 20 cm. Initially, a boat is gently placed by hand at one end of the tank. Its motion is then recorded by a camera located above the tank, with a frame rate of 5 fps. After 180 s, the boat is taken out of the water. The boat weighs typically 3g less after each launch, which corresponds to the amount of mass dissolved during the experiment. Measurements are performed between 3 and 5 times for each boat at which point the decrease of the size of the candy plate ceases to be negligible, and the dissolving slab is replaced.

Data, materials, and software availability

621

622

623

624

625

626

630

631

633

634

636

637

638

639

641

642

643

644

645

646

647

648

649

650

651

652

653

654

655

656

657

658

659

660

661

662

666

667

668

669

670

671

673

674 675

680

681

All study data are included in the article, in SI Appendix or in Datasets S1 to S10.

ACKNOWLEDGMENTS. We thank Sylvain Courrech du Pont (Université Paris Cité) and Olivier Devauchelle (IPG Paris) for scientific discussions, as well as Animesh Biswas (Clark University) for help in performing these experiments. This research was partially funded by the ANR grant Erodiss ANR-16-CE30-0005, and U.S. NSF Grant No. CBET-1805398. M.C. and M.B. acknowledge the hospitality of the Department of Physics at Clark University while the initial experiments were developed and performed.

- 1. Marchetti MC, et al. (2013) Hydrodynamics of soft active matter. Rev. Mod. Phys. 85(3):1143-
- 2. Brennen C, H. Winet H (1977) Fluid mechanics of propulsion by cilia and flagella. Annual Review of Fluid Mechanics 9(1):339-398.
- 3. Lauga E, Powers TR (2009) The hydrodynamics of swimming microorganisms. Reports on Progress in Physics 72(9):096601.
- Elgetti J, Winkler RG, Gompper G (2015) Physics of microswimmers-single particle motion and collective behavior: a review. Reports on Progress in Physics 78(5):056601.
- Jee AY, Cho YK, Granick S, Tlusty T (2018) Catalytic enzymes are active matter. Proceedings
- of the National Academy of Sciences 115(46):E10812-E10821. Dorbolo S, Volfson D, Tsimring L, Kudrolli A (2005) Dynamics of a bouncing dimer. Phys. Rev.
- Lett. 95(4):044101 Kudrolli A, Lumay G, Volfson D, Tsimring LS (2008) Swarming and swirling in self-propelled
- polar granular rods. Phys. Rev. Lett. 100(5):058001. 8. Golestanian R, Liverpool TB, Ajdari A (2005) Propulsion of a molecular machine by asymmetric
- distribution of reaction products. Phys. Rev. Lett. 94(22):220801. Izri Z, van der Linden MN, Michelin S, Dauchot O (2014) Self-propulsion of pure water droplets
- by spontaneous marangoni-stress-driven motion. Phys. Rev. Lett. 113(24):248302. 10. Maass CC, Krüger C, Herminghaus S, Bahr C (2016) Swimming droplets. Annu. Rev. Condens.
- Matter Phys. 7(1):171-193.
- 663 11. S.Ryazantsev Y, et al. (2017) Thermo- and soluto-capillarity: Passive and active drops. Advances in Colloid and Interface Science 247:52-80. 664 665
 - Reichert B, Cam JBL, Saint-Jalmes A, Pucci G (2021) Self-propulsion of a volatile drop on the surface of an immiscible liquid bath. Phys. Rev. Lett. 127(14):144501.
 - 13. Linke H, et al. (2006) Self-propelled leidenfrost droplets. Phys. Rev. Lett. 96(15):154502.
 - Lagubeau G, Merrer ML, Clanet C, Quéré D (2011) A liquid droplet placed on a hot surface can levitate, and moreover, self-propel if the surface is textured. solids can similarly self-propel Nature Physics 7(5):395-398
 - Gauthier A, Diddens C, Proville R, Lohse D, van der Meer D (2019) Self-propulsion of inverse leidenfrost drops on a cryogenic bath. Proceedings of the National Academy of Sciences
 - Allshouse MR, Barad MF, Peacock T (2010) Propulsion generated by diffusion-driven flow. Nature Physics 6(7):516-519.
- 17. Mercier MJ, Ardekani AM, Allshouse MR, Doyle B, Peacock T (2014) Self-propulsion of 677 immersed objects via natural convection. Phys. Rev. Lett. 112(20):204501.
- 18. Sullivan TS, Liu Y, Ecke RE (1996) Turbulent solutal convection and surface patterning in solid 678 dissolution. Phys. Rev. E 54(1):486-495
 - 19. Davies Wykes MS, Huang JM, Hajjar GA, Ristroph L (2018) Self-sculpting of a dissolvable body due to gravitational convection. Physical Review Fluids 3:043801.

20. Philippi J. Berhanu M. Derr J. Courrech du Pont S (2019) Solutal convection induced by dissolution. Phys. Rev. Fluids 4(10):103801.

682

683

684

685

686

687

688

689

690

691

692

693

694

695

696

697

698

699

700

701

702

703

704

705

707

709

710

712

713

714

715

716

717

718

719

720

721

722

723

724

725

726

727

728

729

730

731

732

733

734

735

736

737

738

739

740

741

742

743

744

745

746

747

748

749

750

751

752

- Cohen C, Berhanu M, Derr J, Courrech du Pont S (2020) Buoyancy-driven dissolution of inclined blocks: Erosion rate and pattern formation. Phys. Rev. Fluids 5(5):053802.
- 22. Huang JM, Tong J, Shelley M, Ristroph L (2020) Ultra-sharp pinnacles sculpted by natural convective dissolution. PNAS 117:23339-23344
- Dorbolo S, et al. (2016) Rotation of melting ice disks due to melt fluid flow. Phys. Rev. E 93(3):033112.
- 24. Chamolly A, Lauga E (2019) Stochastic dynamics of dissolving active particles. The European Physical Journal E 42(7).
- 25. Mountain DG (1980) On predicting ice drift. Cold Regions Science and Technology 1(3-4):273.
- Andersson LE, Scibilia F, Imsland L (2016) An estimation-forecast set-up for iceberg drift prediction. Cold Regions Science and Technology 131:88-107.
- Feltham D (2008) Sea ice rheology. Annual Review of Fluid Mechanics 40:91-112.
- Alberello A, et al. (2020) Drift of pancake ice floes in the winter antarctic marginal ice zone during polar cyclones. Journal of Geophysical Research: Oceans 125(3):e2019JC015418.
- 29. Nakata S, et al. (1997) Self-rotation of a camphor scraping on water: new insight into the old problem. Langmuir 13(16):4454-4458.
- 30. Nagayama M, Nakata S, Doi Y, Hayashima Y (2004) A theoretical and experimental study on the unidirectional motion of a camphor disk. Physica D: Nonlinear Phenomena 194(3-4):151-
- Biswas A, Cruz J, Parmananda P, Das D (2020) First passage of an active particle in the presence of passive crowders. Soft Matter 16(26):6138-6144.
- Lide DR, ed. (2004) The Handbook of Chemistry and Physics. (CRC Press).
- Vella D, Mahadevan L (2005) The "cheerios effect". American Journal of Physics 73(9):817-825
- Dalbe MJ, Cosic D, Berhanu M, Kudrolli A (2011) Aggregation of frictional particles due to 34. capillary attraction. Physical Review E 83:051403
- 35. Gazzola M, Argentina M, Mahadevan L (2014) Scaling macroscopic aquatic locomotion. Nature Physics 10(10):758-761
- Gazzola M, Argentina M (2015) Gait and speed selection in slender inertial swimmers. Proceedings of the National Academy of Sciences 112(13):3874-3879.
- Van Buren T, Floryan D, Wei N, Smits AJ (2018) Flow speed has little impact on propulsive characteristics of oscillating foils. Physical Review Fluids 3(1):013103.
- Guyon E, Hulin JP, Petit L, Mitescu CD (2015) Physical Hydrodynamics, 2nd Edition. (Oxford, University Press)
- Brennen CE (2006) An Internet Book on Fluid Dynamics. (Dankat Publishing.).
- Brennen CE (1982) A review of added mass and fluid inertial forces, (aval Civil Eng. Lab., Port Hueneme, Calif., Report CR82.010), Technical report.
- Sharma RS, Berhanu M, Kudrolli A (2022) Alcove formation in dissolving cliffs driven by density inversion instability. Physics of Fluids 34(5):054118.
- 42. Pegler SS, Davies Wykes MS (2020) Shaping of melting and dissolving solids under natural convection. J. Fluid Mech. 900:A35.
- 43. Chandrasekhar S (1961) Hydrodynamic and Hydromagnetic Stability. (Clarendon Press, Oxford).
- Schlichting H (1979) Boundary layer theory. (McGraw-Hill).
- Meakin P, Jamtveit B (2010) Geological pattern formation by growth and dissolution in aqueous systems. Proc. R. Soc. A 466:659-694.
- Cohen C, Berhanu M, Derr J, Courrech du Pont S (2016) Erosion patterns on dissolving and melting bodies (2015 gallery of fluid motion). Phys. Rev. Fluids 1(5):050508.
- Kerr RC (1994) Melting driven by vigorous compositional convection. Journal of Fluid Mechanics 280(1):255-285.
- Kerr RC (1994) Dissolving driven by vigorous compositional convection. Journal of Fluid 48. Mechanics 280(1):287-302
- Hewitt IJ (2020) Subglacial plumes. Annual Review of Fluid Mechanics 52(1):145-169.
- McConnochie CD, Kerr RC (2016) The turbulent wall plume from a vertically distributed source of buoyancy. Journal of Fluid Mechanics 787:237-253.
- 51. McKenna R (2005) Iceberg shape characterization in Proceedings 18th International Conference on Port and Ocean Engineering under Arctic Conditions. Vol. 2, pp. 555-564.
- Cenedese C, Straneo F (2023) Icebergs melting. Annual Review of Fluid Mechanics 55
- 53. Romanov YA, Romanova NA, Romanov P (2012) Shape and size of antarctic icebergs derived from ship observation data. Antarctic Science 24(1):77-87.
- Weady S, Tong J, Zidovska A, Ristroph L (2022) Anomalous convective flows carve pinnacles and scallops in melting ice. Physical Review Letters 128(4):044502.
- Bohleber P, et al. (2017) Ground-penetrating radar reveals ice thickness and undisturbed englacial layers at kilimanjaro's northern ice field. The Cryosphere 11(1):469-482.
- Zhou M, Bachmayer R, deYoung B (2019) Mapping the underside of an iceberg with a modified underwater glider. Journal of Field Robotics 36(6):1102-1117
- Wagner TJ, Dell RW, Eisenman I (2017) An analytical model of iceberg drift. Journal of Physical Oceanography 47(7):1605-1616.
- Marchenko A, Diansky N, Fomin V (2019) Modeling of iceberg drift in the marginal ice zone of the barents sea. Applied Ocean Research 88:210-222.